J Physiol 596.21 (2018) pp 5281–5298

The Journal of Physiology

Complex and spatially segregated auditory inputs of the mouse superior colliculus

Veronika Bednárová[1,2,3], Benedikt Grothe[1,2,3] and Michael H. Myoga[1,2,3]

[1] *Max Planck Fellow Group: Circuits of Spatial Hearing, Max Planck Institute of Neurobiology, 82152 Planegg-Martinsried, Germany*
[2] *Division of Neurobiology, Department Biologie II, Ludwig-Maximilians-Universität München, 82152 Planegg-Martinsried, Germany,*
[3] *Graduate School of Systemic Neurosciences, Ludwig-Maximilians-Universität München, 82152 Planegg-Martinsried, Germany,*

Edited by: Ian Forsythe & Andrew King

Key points

- Although the visual circuits in the superior colliculus (SC) have been thoroughly examined, the auditory circuits lack equivalent scrutiny.
- SC neurons receiving auditory inputs in mice were characterized and three distinguishable types of neurons were found.
- The auditory pathways from external nuclei of the inferior colliculus (IC) were characterized, and a novel direct inhibitory connection and an excitation that drives feed-forward inhibitory circuits within the SC were found.
- The direct excitatory and inhibitory inputs exhibited distinct arbourization patterns in the SC.
- These findings suggest functional differences between excitatory and inhibitory sensory information that targets the auditory SC.

Abstract The superior colliculus (SC) is a midbrain structure that integrates auditory, somatosensory and visual inputs to drive orientation movements. While much is known about how visual information is processed in the superficial layers of the SC, little is known about the SC circuits in the deep layers that process auditory inputs. We therefore characterized intrinsic neuronal properties in the auditory-recipient layer of the SC (stratum griseum profundum; SGP) and confirmed three electrophysiologically defined clusters of neurons, consistent with literature from other SC layers. To determine the types of inputs to the SGP, we expressed Channelrhodopsin-2 in the nucleus of the brachium of the inferior colliculus (nBIC) and external cortex of the inferior colliculus (ECIC) and optically stimulated these pathways while recording from SGP neurons. Probing the connections in this manner, we described a monosynaptic excitation that additionally drives feed-forward inhibition via circuits intrinsic to the SC. Moreover, we found a profound long-range monosynaptic inhibition in 100% of recorded SGP neurons, a surprising finding considering that only about 15% of SGP-projecting neurons in the nBIC/ECIC are inhibitory. Furthermore, we found spatial differences in the cell body locations as well as axon trajectories

Veronika Bednárová completed an Anatomy, Developmental and Human Biology BSc degree at Kings College London in 2012, where the neuroanatomy courses steered her toward neuroscience. Since 2014 she has been enrolled in a PhD program at the Graduate School of Systemic Neurosciences (GSN) in Munich. Currently, she is completing her GSN doctoral degree under the supervision of M.H.M. and B.G. B.G.'s scientific openness allowed her to explore the brain circuits of spatial hearing. She is aspiring to become a postdostocal researcher and to stay in academic research.

DOI: 10.1113/JP276370

between the monosynaptic excitatory and inhibitory inputs, suggesting that these inputs may be functionally distinct. Taking this together with recent anatomical evidence suggesting an auditory excitation from the nBIC and a GABAergic multimodal inhibition from the ECIC, we propose that sensory integration in the SGP is more multifaceted than previously thought.

(Received 27 April 2018; accepted after revision 10 September 2018; first published online 19 September 2018)
Corresponding author: M. H. Myoga and B. Grothe Max Planck Fellow Group: Circuits of Spatial Hearing, Max Planck Institute of Neurobiology, Am Klopferspitz 18, 82152 Planegg-Martinsried, Germany. Email: mmyoga@neuro.mpg.de and grothe@lmu.de

Introduction

The manner in which animals integrate sensory information across modalities is crucial to their ability to navigate their environment. The superior colliculus (SC) is a midbrain structure that is important for executing sensory-evoked orientation movements. It integrates auditory, somatosensory and visual inputs and translates them into motor commands to orient the head and the upper body towards salient objects in space. While recent studies have provided specific insights into how the neurons and the circuits of the SC process visual information (Gale & Murphy, 2014, 2016; Ahmadlou & Heimel, 2015; Feinberg & Meister, 2015; Inayat *et al.* 2015), the identity of the auditory-recipient SC neurons and the nature of their synaptic inputs are currently unknown.

The SC is a layered structure, where visual inputs enter the superficial layers (stratum griseum superficiale, SGS; stratum opticum, SO), somatosensory and auditory inputs enter the innermost layers (stratum griseum profundum, SGP), and motor output commands are generated in the intermediate layers (stratum griseum intermediale, SGI; stratum album intermediale, SAI) (May, 2005). While the nomenclature of the SC laminae varies across literature, in this study we employed that of Helms *et al.* (2004), which is often used in other SC electrophysiological studies (Saito & Isa, 1999). Previous studies have investigated the cell types in the superficial (Gale & Murphy, 2014) and intermediate layers (Saito & Isa, 1999), with at least six electrophysiologically defined classes of neurons in the intermediate layers. In contrast, the electrophysiological profile of the auditory-recipient neurons in the SGP layer of the SC is not known.

Anatomical studies have shown that the majority of SC auditory inputs arise from neurons in the nucleus of the brachium of the inferior colliculus (nBIC) and the lateral side of the external cortex of the inferior colliculus (ECIC; sometimes referred to as the lateral cortex of the inferior colliculus, IClc, or the external nucleus of the inferior colliculus, ICx) (Edwards *et al.* 1979; Druga & Syka, 1984; Covey *et al.* 1987; Jiang *et al.* 1997; Doubell *et al.* 2000). These neurons receive auditory inputs mainly from the central nucleus of the inferior colliculus (ICc) (Aitkin & Phillips, 1984) and in turn project predominantly to the innermost layer of the ipsilateral SC (the SGP). Although many studies have investigated the auditory spatial coding strategies of the nBIC/ECIC–SC circuit (Palmer & King, 1982; Middlebrooks & Knudsen, 1984; King & Hutchings, 1987), much less attention was devoted to the underlying circuit elements. One study, using electrical stimulation of the nBIC and current-clamp recordings in the SC, described an excitatory connection (Skaliora *et al.* 2004). However, a recent tracing study has also demonstrated a small population of putative direct inhibitory connections originating in the nBIC/ECIC (Mellott *et al.* 2018), suggesting that the connections between the nBIC/ECIC and SGP-residing neurons in the SC may be more complex than originally thought.

We therefore developed an *in vitro* preparation to investigate the synaptic connectivity between the nBIC/ECIC and the SGP of the mouse, which offers the convenience of combining optogenetic manipulations with whole-cell electrophysiology. We confirmed three distinguishable classes of SGP neurons, which resemble types of neurons found in other SC layers. All neurons were innervated by a direct excitatory connection, but also a direct inhibitory connection, a surprising finding considering the mere 15% of SC-projecting GABAergic neurons reported in the nBIC/ECIC in our study and 10% in Mellott *et al.* (2018). Histological analysis indicates that the majority of these neurons are parvalbumin positive. Channelrhodopsin (ChR2)-assisted circuit mapping and retrograde anatomical tracing further revealed distinct excitatory and inhibitory projection trajectories to the SGP and cell body distributions, respectively, suggesting a functional segregation between the direct excitatory and inhibitory inputs.

Methods

Ethical approval

All experimental procedures were carried out in compliance with German animal welfare law (Tierschutzgesetz), approved by the regional authority (Regierung von Oberbayern) under file no. 55.2-1-54-2532.0-91-14 and conform to the principles and regulations as described in the editorial by Grundy (2015). A total of 32 male and female mice (C57BL/6) were used in this study. All originated from the in-house

Table 1. Coordinates of stereotactic injections

Substance	Titre/dilution	Amount	AP	ML	DV	Target
AAV2/1.hSyn.ChR2(H134R).eYFP.WPRE.hGH	5.86×10^{16}	0.1 μl	−4.36	−1.6	2.46	nBIC/ECIC
Hydroxystilbamidine bis(methanesulfonate)	5% in ddH_2O	0.2 μl	−4.1	−0.77	2.21	SGP

Coordinates (in mm) are relative to bregma. AP, anteroposterior; DV, dorsoventral; ML, mediolateral.

mouse facility at the Max Planck Institute of Neurobiology. At all times the mice had access to fresh water and food *ad libitum* and were kept under 12/12 h light/dark cycles.

Stereotactic injections

Mice aged postnatal day 24 were anaesthetized with an intraperitoneal injection of a mixture of fentanyl (0.05 mg kg^{-1}), midazolam (5 mg kg^{-1}) and medetomidine (0.5 mg kg^{-1}). Each mouse also received an oral dose of the analgesic metamizole (200 mg kg^{-1}), and a subcutaneous injection of carprofen (5 mg kg^{-1}) as an anti-inflammatory agent. Mice were fitted onto a stereotaxic frame of a Microinjection Robot (Neuro-Star, Tübingen, Germany). The eyes were covered with Isopto-Max eye cream (Alcon Pharma, Freiburg, Germany) for its antiexudative effect to prevent corneal drying, and the skin of the skull was locally anaesthetized using 10% lidocaine. The animal's physiological body temperature was maintained using a heating pad warmed to 37°C, which was designed and assembled by the in-house electronics facility. The animal's skin was cut and a small hole over the target brain area was drilled using a steel bur (ref. no. 310 104 001 001 004, Hager & Meisinger GmbH, Neuss, Germany) powered by Micro Motor Kit 1045 (Foredom, Bethel, CT, USA). Viruses or retrograde tracers were then injected into the target area using a 10 μl NanoFil syringe (World Precision Instruments, Sarasota, FL, USA) at the rate of 0.05 μl min^{-1}. For retrograde tracing experiments, 0.2 μl Fluoro-Gold (hydroxystilbamidine bis(methanesulfonate), Sigma-Aldrich) was injected into the SGP layer of the SC. For electrophysiological experiments, 0.1 μl of AAV2/1.hSyn.ChR2(H134R).eYFP.WPRE.hGH (titre: 5.86×10^{16}, pAAV-hSyn-hChR2(H134R)-EYFP was a gift from Karl Deisseroth (Addgene plasmid no. 26973), University of Pennsylvania Vector Core) was injected into the nBIC/ECIC. The human synapsin (hSyn) promotor used in this study has been shown to be expressed in both excitatory and inhibitory neurons in the mouse cortex (Nathanson *et al.* 2009) and under our experimental conditions the adeno-associated virus (AAV) 2/1 efficiency was 83% (2 out of 12 nBIC/ECIC neurons were negative for eYFP.ChR2), as determined by whole-cell recordings and somatic optical stimulation. Details on specific injection coordinates are provided in Table 1. The syringe was kept in place for 2 min after the injection to allow the substance to diffuse within the brain and was then slowly withdrawn. Finally, the skin of the skull was sutured using K802 Perma-hand Silk (Ethicon, Somerville, NJ, USA), and the animal was injected subcutaneously with an antidote mixture of naloxone (1.2 mg kg^{-1}), flumazenil (0.5 mg kg^{-1}) and atipamezole (2.5 mg kg^{-1}) to end the anaesthesia. After the surgery no antibiotics were administered, but on the first day after the surgery a subcutaneous injection of carprofen (5 mg kg^{-1}) for anti-inflammatory purposes was administered. The mouse recovery was observed for two consecutive days after the surgery and thereafter every third day until the day of the *in vitro* (2 weeks post-surgery) or histological experiments (4 days post-surgery).

Acute superior colliculus slices

Two weeks after the injection of the virus, mice were anaesthetized with 1 ml isofluorane (2-chloro-2-(difluoromethoxy)-1,1,1-trifluoroethane), placed in a 2.4 l induction chamber and decapitated. The brain tissue was immediately placed into an ice-cold (~4°C) dissecting solution containing the following (in mM): 73 sucrose, 83.8 NaCl, 24 $NaHCO_3$, 1.25 NaH_2PO_4, 2.5 KCl, 25 D-glucose, 4 $MgCl_2$, 0.5 $CaCl_2$ (pH 7.49 when bubbled with 95% O_2 and 5% CO_2). Coronal SC slices (300 μm thick) were prepared using a VT 1200S vibrating-blade microtome (Leica, Wetzlar, Germany). The slices that were collected originated from regions −4.72 to −4.16 mm relative to bregma (Franklin & Paxinos, 2007). The slices were then incubated for ~20 min at 35°C in an artificial cerebrospinal fluid (aCSF) containing the following (in mM): 128.3 NaCl, 2.5 KCl, 2 $MgCl_2$, 1.25 NaH_2PO_4, 26 $NaHCO_3$, 2 $CaCl_2$, 10 D-glucose (pH 7.48 when bubbled with 95% O_2 and 5% CO_2), after which they were transferred to the recording chamber.

Electrophysiology

All experiments were performed in perfused aCSF (flow-rate 1 ml min^{-1}, bubbled with 95% O_2 and 5% CO_2). Recording temperature was measured near the slice and maintained at 30°C by an SH-27B in-line heater (Warner Instruments, Hamden, CT, USA) powered by a TC-324C heater controller (Warner Instruments). The tissue was visualized under an Eclipse FN1 upright microscope (Nikon, Minato, Japan) equipped with

custom-built Dodt gradient contrast optics, a D-CUO DIC oil condenser (Nikon) and a Retiga EXi camera (QImaging, Surrey, Canada). Whole-cell recordings of SGP neurons, defined as <200 μm dorsal from the central grey (CG), were obtained under visual control using a 60× (0.90 NA) water immersion objective (Olympus, Shinjuku, Japan) with borosilicate glass electrodes using a MultiClamp 700B amplifier (Molecular Devices, San Jose, CA, USA). Data were acquired at 10 kHz and were not low-pass filtered below this frequency. Analysis was performed offline using MATLAB (The Mathworks, Natick, MA, USA). Recording electrodes were filled with a potassium gluconate based internal solution containing the following (in mM): 144 potassium gluconate, 4 KCl, 10 Hepes, 10 Na_2-phosphocreatine, 4 Mg-ATP, 0.3 Na_2-GTP, 0.05 Alexa Fluor 594 (Thermo Fisher Scientific, Waltham, MA, USA), adjusted to pH 7.3 (at 30°C) and 296 mOsm. Electrodes had 3.8–4.2 MΩ tip resistances. Recordings were accepted only if the uncompensated series resistance was <20 MΩ and stable over the course of the recording (<20% change).

Current-clamp experiments

For intrinsic electrophysiological property measurements, hyperpolarizing and depolarizing current steps of 250 ms duration were delivered through the recording electrode to the neurons, and their membrane responses were recorded in the current-clamp configuration. Depending on the input resistance of the neuron, the hyperpolarizing steps ranged from −100 to 0 pA (10 pA per step) or from −50 to 0 pA (5 pA per step). The depolarizing steps ranged from 0 to 700 pA (50 pA per step). To induce single action potentials (APs), short depolarizing current steps with 10 ms duration and with a range of 25–250 pA (25 pA per step) were delivered, and the APs from these recordings were used to construct phase-plane plots.

Laser stimulation set-up

ChR2-expressing presynaptic neurons were optically stimulated with 473 nm light from an S3FC473 solid-state laser (ThorLabs) coupled to an RB42F1 optic fibre and an F230FC-A collimator (ThorLabs, Newton, NJ, USA). The laser pulses were directed via an OPX2250 galvanometer-based scanhead (ThorLabs) to the back aperture of a 4× (0.13 NA) air objective (Nikon) focused on the brain slice. The laser spot size was ∼300 μm (full width at half-maximum). This beam was intentionally designed to have a pencil shape, providing better uniform illumination through the slice, but at the expense of diameter, which is larger than what an overfilled 0.13 NA objective would produce. The intensity of the light pulses was modulated directly via the 473 nm laser controller and additionally gated with a VS-14 shutter (Uniblitz, Rochester, NY, USA). Data acquisition was controlled using open source software Ephus (Suter *et al.* 2010) running on MATLAB.

Voltage-clamp/photostimulation experiments

For ChR2-assisted circuit mapping experiments (Petreanu *et al.* 2007), laser pulses (2 ms duration, 1 s inter-stimulus interval) were delivered on an 8 × 8 stimulation grid with 175 μm spacing. This stimulation grid area (1.2 × 1.2 mm) was sufficient to cover both the nBIC and the ECIC. Due to the relatively large laser spot size, activation sometimes bled into a neighbouring position, but seldom any further. The closest laser stimulation point was >400 μm away from the SGP neuron recorded, and the recordings were always performed in the SC hemisphere ipsilateral to the injection site. Neurons were voltage-clamped at −70 and 0 mV to measure excitatory postsynaptic currents (EPSCs) and inhibitory postsynaptic currents (IPSCs), respectively. The EPSCs and IPSCs recorded by stimulation of a particular stimulation grid position were used to construct excitatory and inhibitory synaptic input maps. Each recording was repeated 3–5 times under control conditions, after which 5 μM (*R*)-4-(3-phosphonopropyl)piperazine-2-carboxylic acid ((*R*)-CPP) and 10 μM 2,3-dihydroxy-6-nitro-7-sulfamoyl-benzo(*f*)chinoxalin-2,3-dione (NBQX, Tocris, Bristol, UK) were perfused through the chamber to block NMDA and AMPA receptors, respectively. After 2 min of drug perfusion (from the moment the aCSF with the drugs entered the recording chamber) the inhibitory (repeated 3–5 times) and excitatory (repeated once) recordings were acquired again. To block $GABA_A$ receptors, 20 μM picrotoxin (Tocris) was perfused through the slice. This perfusion protocol was empirically tested in our laboratory to completely block each receptor of interest in this study. The laser intensity (0.06–0.88 mW) was kept constant throughout the experiment. Data from these experiments were used for distributions analysis, IPSC peak analysis (to distinguish polysynaptic from monosynaptic inputs), latency analysis and the strength of direct inhibition on cell clusters ($n = 10$ SGP neurons).

Synaptic current analysis

For each stimulus position, the EPSC/IPSC strength was calculated as the peak response current of the averaged traces in a time window of 1–21 ms after the stimulus onset. EPSCs and IPSCs were considered non-zero if their amplitudes were larger than 7 times the SD of a 20 ms baseline directly before stimulus onset. Since we do not know the number of nBIC/ECIC projections of a given SGP neuron and how many of those were infected by the AAVs, it is challenging to compare their strengths onto the same SGP neuron (Petreanu *et al.* 2009). Thus, the synaptic input maps were normalized.

To compare amplitude differences due to blocking of NMDA and AMPA receptors, the maps obtained from recordings during blockade of excitatory transmission were normalized to the maximal value of their respective control input maps (drug inhibition normalized to control inhibition, drug excitation normalized to control excitation). To plot mediolateral and dorsoventral input distribution profiles, the synaptic input maps were collapsed by taking the maximal response along the mediolateral or dorsoventral dimension and then averaged across 10 SGP neurons. Half-maximal response positions were interpolated from cumulative distributions of these profiles (data presented as mean ± SEM), and the nonparametric Kruskal–Wallis test was used to check for statistical significance between the distributions of the half-maximal positions. For latency analysis, only the grid stimulus positions within the nBIC/ECIC which evoked EPSCs and IPSCs were considered, and from those a mean direct inhibitory and excitatory latency for a single cell was calculated and then averaged across five SGP neurons which fit that criteria. Latency data are presented as mean ± SEM in the Results section.

Distinguishing polysynaptic and monosynaptic inhibitory inputs

In some preparations, no currents could be measured when stimulating the nBIC/ECIC, likely due to somas severed from their axons during the slicing process or slightly different cutting angles. In these cases, the grid (either an 8 × 8 grid, 175 μm spacing or a 4 × 4 grid, 200 μm spacing) was moved dorsomedially to map the axons of the nBIC/ECIC neurons running into the SGP. Thus, in these recordings, the closest stimulation point in some cases was less than 100 μm from the recorded SGP neuron ($n = 15$ SGP neurons). Data from these experiments were used for IPSC peak analysis and for calculating the strength of direct inhibition on cell type clusters (in total 25 SGP neurons). To distinguish polysynaptic from monosynaptic IPSCs, the peaks of the three individual recording traces were compared between control and drug wash-in conditions using Kruskal–Wallis tests, and this was performed for every non-zero grid position for all recordings regardless of grid location. If a single position within the grid map showed a significant decrease ($P < 0.05$) in IPSC peak value after drug wash-in, the SGP neuron was considered to have a polysynaptic inhibitory component. Otherwise, the SGP neuron was considered to have predominantly monosynaptic inhibitory connections.

Analysis of intrinsic electrophysiological properties

Five electrophysiological parameters were calculated from membrane responses to the hyperpolarizing and depolarizing current steps. Hyperpolarizing steps producing a small hyperpolarization (−10 to −5 mV) from the resting membrane potential were used to determine the input resistance (R_m). Maximum firing frequency was calculated in hertz from the 700 pA depolarizing current step. Some neurons exhibited a 'late-spiking' property, which was calculated as the ratio of the inter-spike interval (ISI) between the first and second AP (ISI_1) to the ISI between the second and the third AP (ISI_2). The time (in milliseconds) from the current step onset to the first AP (time to spike) and AP width at half-amplitude (spike half-width) were measured at the AP threshold depolarizing current step. Data are presented as mean ± SD. For cluster analysis, we used Euclidean distance and shortest distance linkage criteria for hierarchical clustering. Here, each data parameter was normalized between 0 (population minimum) and 1 (population maximum). An alternative clustering algorithm *k*-means was also performed to compare with the hierarchical clustering results. With three predefined number of clusters, the clusters were well separated (silhouette value >0.5 included 21/23 neurons), while with four predefined number of clusters, one neuron had a negative silhouette value (silhouette value >0.5 included 17/23 neurons). This indicates poor cluster separation when more than three clusters were tested, corroborating our linkage-distance criterion. From the 25 SGP neurons recorded with presynaptic ChR2 stimulation, intrinsic electrophysiological characterization was obtained for 19. These neurons were separately classified into the three clusters using the same clustering method as described above.

Analysis of the strength of direct inhibition on SGP cell clusters

For this analysis, 19 SGP neurons and their corresponding inhibitory input maps in the NMDA/AMPA blocked condition were analysed. Here we analysed the IPSC amplitudes either cell type-wise or stimulation position-wise. In the cell type-wise analysis, we first calculated the mean IPSC value of an inhibitory input map of each cell. The mean values were then separated into three clusters, according to the cell type cluster to which the cells were allocated by hierarchical clustering. In the stimulation position-wise analysis, we calculated all IPSC amplitudes evoked by multiple stimulation positions for each cell, and these were then segregated according to the cluster to which the cells were allocated by hierarchical clustering. To test for statistical differences between cell clusters on either the cell type-wise or stimulation position-wise IPSC amplitudes, we used a two-sample Kolmogorov–Smirnov test.

Table 2. List of main reagents used for immunohistochemistry

		Working dilution	Source	Catalogue no.
Primary antibody	Host			
Anti-GAD67	Mouse	1:200	Abcam	Ab26116
Anti-parvalbumin	Rabbit	1:500	Swant	SV28
Anti-calretinin	Rabbit	1:500	Swant	7699/3H
Anti-calbindin D-28k	Rabbit	1:500	Swant	CB38a
Anti-choline acetyltransferase	Goat	1:500	Millipore	AB144P
Anti-somatostatin	Rat	1:100	Millipore	MAB354
Secondary antibody	Conjugated to			
Anti-mouse	Alexa488	1:200	Dianova	715-545-150
Anti-rabbit	CY3	1:400	Dianova	711-165-152
Anti-goat	CY3	1:300	Dianova	705-165-147
Anti-rat	CY3	1:400	Dianova	712-165-153
Deep-Red Nissl stain	—	1:100	Thermo Fisher Scientific	N21483

Sources: Abcam, Cambridge, UK; Swant, Marly, Switzerland; Millipore, Burlington, MA, USA; Dianova, Hamburg, Germany; Thermo Fisher Scientific, Carlsbad, CA, USA.

Analysis of somatodendritic morphology

After the recordings (10 min minimum time of dye diffusion), dendritic arbours of 20 SGP neurons filled with Alexa Fluor 594 (50 μM in the recording pipette) were imaged using an Acera resonant-galvanometer two-photon scanhead (Thorlabs) driven by a Mai Tai eHPDS ti:sapphire laser (Spectra-Physics, Santa Clara, CA, USA). Tracing was performed on *z*-stacks (30 frames averaged, 1 μm step size) and the three dimensions of the dendrites were measured. To calculate the arbour orientation index (AOI) (Gale & Murphy, 2014), the vertical axis of the neuron was determined as the angle of the vector producing the shortest distance from the neuron soma to the dorsal surface of the SC. Two lines intersecting at the soma with a $\pm 45°$ angle from the vertical axis were then drawn, dividing the dendritic arbour into four quadrants: dorsal, ventral, lateral and medial. Sholl analysis (Sholl, 1953) was then used to measure the number and locations of dendrite intersections with circles of increasing radii (25 μm/circle) from the centre of the soma. The AOI was then calculated according to:

$$\mathrm{AOI} = \frac{\text{Sholl V} - \text{Sholl H}}{\text{Sholl V} + \text{Sholl H}} \quad (1)$$

where the number of Sholl points in the dorsal and ventral quadrant was added together to make the number of points in the vertical axis (Sholl V) and the lateral and medial were added to make the horizontal axis (Sholl H). Indices near 1 indicate a dorsoventral orientation along the vertical axis, and indices close to 0 indicate branches oriented equally in all directions. AOI data are presented as means ± SD. The same Sholl analysis was used to determine the number of primary dendrite branches from the soma, and the data are presented as mean ± SD.

Immunohistochemistry

For retrograde tracing experiments, three mice received a monolateral injection of Fluoro-Gold into their SGP layer of the SC. Four days after retrograde tracer injection, the mice were anaesthetized and decapitated using the same isoflurane anaesthesia procedure for acute electrophysiology experiments. The dissected brain was placed into 4% paraformaldehyde in 0.2 M phosphate buffered saline (PBS) for 3 h at room temperature and then overnight at 4°C. Before slicing, the brain was washed 3 times in 0.02 M PBS and embedded in 4% agar (in H_2O). Then, coronal brain sections of 50 μm were collected on a VT 1200S vibrating-blade microtome. After rinsing in 0.02 M PBS, sections were placed into a blocking solution containing 1% bovine serum albumin, 0.5% Triton X-100 and 0.1% saponin in PBS. The slices were incubated overnight at 4°C with primary antibodies and for 3 h at room temperature with secondary antibodies. Antibody specifications are listed in Table 2. Slices from all three brains were used for glutamic acid decarboxylase of molecular mass 67 kDa (GAD67), calretinin, and parvalbumin staining. For calbindin and somatostatin staining, slices from two brains were used, and one of the mice was used for choline acetyltransferase (ChAT) staining. After antibody incubation, sections were rinsed 3 times for 10 min in 0.02 M PBS and cover slipped

with Vectashield mounting medium (Vector Laboratories, Burlingame, CA, USA).

Confocal microscopy

Confocal optical images were acquired with a TCS SP8 confocal microscope (Leica) equipped with an HC PL APO CS2 20× (0.75 NA) glycerol immersion objective. Fluorochromes were visualized with excitation wavelengths of 405 nm for Fluoro-Gold (emission: 530–600 nm), 488 nm for Alexa Fluor 488 (emission: 496–554 nm), 514 nm for CY3 (emission: 520–550 nm), and 633 nm for Deep-Red Nissl (emission: 639–734 nm). Images were acquired as tiles of 738.1 × 738.1 μm (0.72 μm/pixel) and automatically stitched by LAS X software (Leica). All images were Kalman-averaged from two to four successive scans.

Analysis of confocal images and cell counting

Retrogradely labelled neurons were counted in two separate images, one corresponding to the nBIC and the other to the ECIC. Because Fluoro-Gold fluoresced as puncta in the cytoplasm, the retrogradely labelled neurons were distinguished from tissue debris by Nissl counterstaining. The percentages were then calculated according to:

$$\%\ \text{Retro marker} = \frac{\text{Retro marker}}{\text{Retro only} - \text{Retro marker}} \times 100 \quad (2)$$

where the number of counted neurons was labelled as 'Retro only'. The number of those neurons positive for GAD67 or calretinin was labelled as 'Retro GAD67' and 'Retro calretinin', respectively, where the Retro marker was GAD67 or calretinin.

Results

We used wild-type C57BL/6 mice ($N = 10$) to obtain whole-cell current-clamp recordings of 23 SGP neurons. The SGP layer is readily distinguishable from the intermediate layers by markedly lower expression of ChAT (Fig. 1*A*; Chevalier & Mana, 2000), from which we determined the SGP layer to spread up to 200 μm dorsally from the CG and patched exclusively within this region. Neuronal intrinsic electrophysiological properties were obtained by recording the membrane responses to hyperpolarizing and depolarizing current steps (see Methods). Visual inspection of raw traces from these recordings already pointed to at least three distinct electrophysiological types of neurons: spike-adapting (Fig. 1*B*, top), late-spiking (Fig. 1*B*, middle) and fast-spiking (Fig. 1*B*, bottom). To gain further quantitative insight into the electrophysiological diversity of the SGP neurons, we performed hierarchical clustering on the following five parameters: the input resistance, the maximum firing rate (at 700 pA current injections), the ratio of the first to second inter-spike intervals (ISI_1/ISI_2), the time from the current step onset to the first AP (measured at the AP current threshold) and the AP half-widths. We found that the separation between the first three clusters was large (linkage distance: 1.51) relative to the separation between additional clusters (linkage distance 0.98 for four clusters, Fig. 1*C*, top), providing quantitative evidence for at least three distinct SGP neuron types. The cluster separation is visually apparent when plotting each parameter cluster-wise (Fig. 1*D*). Spike-adapting neurons ($n = 6$) had relatively high input resistances (495.7 ± 73.1 MΩ), could not sustain high firing rates (55.3 ± 33.6 Hz) and exhibited relatively broad AP half-widths (0.53 ± 0.14 ms). Late-spiking neurons ($n = 6$) had relatively low input resistances (245.9 ± 51.9 MΩ), large ISI_1/ISI_2 ratios (11.0 ± 4.0) and long latencies to their first AP (175.3 ± 13.1 ms). Fast-spiking neurons ($n = 11$) were able to spike at very high frequencies (336.6 ± 38.1 Hz), exhibited relatively regular ISIs (ISI_1/ISI_2 ratio 1.2 ± 0.61) and had intermediate input resistances (355.2 ± 111.0 MΩ). We did not observe any spatial organization of any cluster type within the area of the SGP from which we recorded (Fig. 1*A*).

We next investigated whether the three neuron clusters also exhibited distinct morphology. To this end, we obtained two-photon *z*-stacks of a subset of recorded neurons (20/23, filled with Alexa Fluor 594 via the patch pipette). Dendritic size was (mean ± SD) 235 ± 81, 300 ± 47 and 67 ± 23 μm in the *x*, *y*, and *z* dimensions, respectively. As the dendritic arbours of all imaged neurons were rather planar and parallel to the coronal slices (20–28% *z*-axis deviation in either the *x* or *y* dimension), we performed further analysis on the *z*-projected micrographs. We also considered the fact that the surface of the SC is curved (along with the individual SC layers) and thus defined the vertical axis for each traced neuron as the angle of the shortest vector that can be drawn between the soma and dorsal surface of the SC, as has been done previously for the superficial SC (Gale & Murphy, 2014). After vertical alignment, the dendritic arbours were segmented into four quadrants representing the dorsoventral and the mediolateral axes. By performing Sholl analysis on each quadrant, we calculated an AOI for each traced neuron, which describes the extent to which dendritic arbours are vertically oriented (Gale & Murphy, 2014, see Methods). Example neurons from each cluster already suggested distinct morphology between the clusters (Fig. 1*E*), where spike-adapting neurons tended to have a vertical orientation, while the late-spiking neurons had typically two dendrites oriented towards the SC surface. In contrast, fast-spiking neurons seemed to have branches in both vertical and horizontal directions in a cross-like manner.

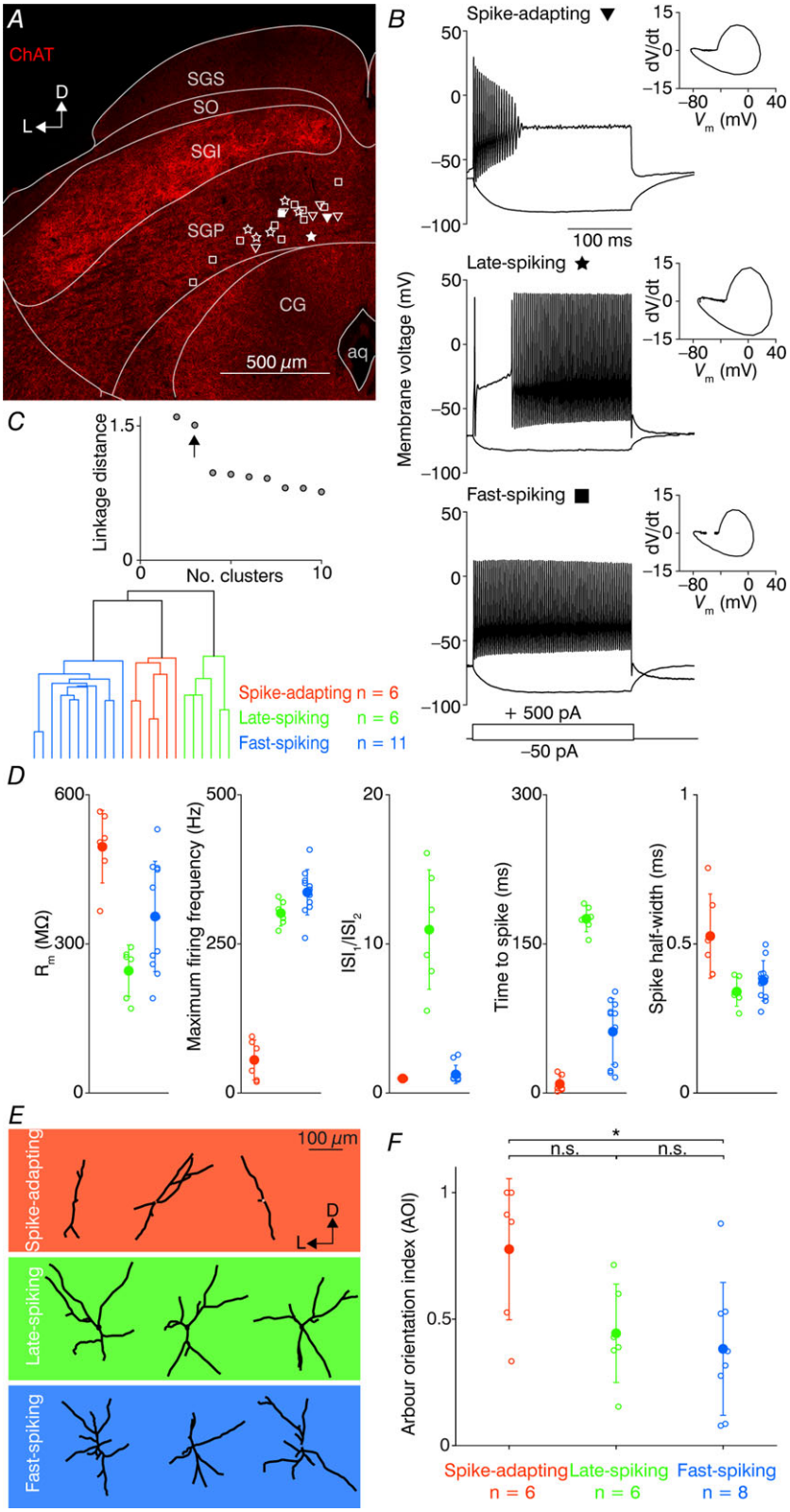

Figure 1. Identification of three SGP neuron types on the basis of their electrophysiological and morphological properties

A, confocal image of a brain slice stained for choline acetyltransferase (ChAT) showing the major divisions of the SC. The locations of all recorded SGP neurons are displayed by open symbols, where triangles correspond to the spike-adapting neurons, stars to the late-spiking neurons and squares to the fast-spiking neurons. The filled symbols are the locations of the representative three SGP neurons shown in *B*. aq, aqueduct; CG, central grey; D, dorsal; L, lateral; SGI, stratum griseum intermediale; SGP, stratum griseum profundum; SGS, stratum griseum superficiale; SO, stratum opticum. *B*, example traces for representative SGP neurons in response to a 250 ms depolarizing (+500 pA) and a hyperpolarizing (−50 pA) current step. Insets show phase-plane plots of the first fired AP. *C*, top, linkage distance of the hierarchical clustering as a function of the increasing cluster number. Arrow indicates the linkage distance for three clusters. Bottom, dendrogram plot of hierarchical binary cluster tree. Colour code in *C* applies to *D*, the background colour in *E*, and *F*. *D*, cluster-wise plots of the following intrinsic parameters (from left to right): input resistance (R_m), maximum firing frequency at the current step of +700 pA, ratio of the first to second inter-spike intervals in a train of APs (ISI_1/ISI_2), time to first spike from the current onset at threshold traces, the half-width of the first fired AP. Open circles represent individual neurons; filled circles represent the cluster mean ± SD. *E*, traced dendrites of three example neurons for each electrophysiologically defined cluster. Orientation axes (L, lateral; D, dorsal) are relative to the dorsal SC surface. *F*, arbour orientation indices (AOIs) of the defined clusters. Open circles represent individual neurons; filled circles represent the cluster mean ± SD. $^*P < 0.05$; n.s., not significant (Kruskal–Wallis test).

Plotting the calculated arbour orientation indices for all neurons (Fig. 1*F*) indeed revealed a higher average value for spike-adapting neurons (0.78 ± 0.28, $n = 6$), compared to late-spikers (0.44 ± 0.20, $n = 6$) and fast-spikers (0.38 ± 26, $n = 8$). The difference between spike-adapting neurons and fast-spikers was also statistically significant ($P = 0.02$, Kruskal–Wallis test). Adding the AOIs into the hierarchical clustering analysis as a sixth parameter did not change the resulting neuron allocation to a specific cluster, but shortened the distance between the late- and fast-spiker clusters (also reflected by the non-significant result for the AOI between late- and fast-spikers, $P = 0.37$, Kruskal–Wallis test). In addition to analysing AOIs, we also counted the number of primary dendritic branches for each cluster (spike-adapting 3.33 ± 1.03, $n = 6$; late-spiking 3.67 ± 0.82, $n = 6$; fast-spiking 4.00 ± 0.76, $n = 8$). In contrast to the AOIs, all clusters had a number of primary dendrites statistically indistinguishable from one another (spike-adapting *vs.* late-spiking, $P = 0.72$; late-spiking *vs.* fast-spiking, $P = 0.41$; spike-adapting *vs.* fast-spiking, $P = 0.23$; Kruskal–Wallis test). Thus, the SGP of the mouse SC is largely populated by three electrophysiologically distinguishable neuronal types that tend to have a characteristic dendritic orientation.

To study the connectivity of the nBIC/ECIC and the SGP we took an optogenetic approach and infected neurons in the nBIC/ECIC with an AAV expressing the light-gated cation channel ChR2, tagged with enhanced yellow fluorescent protein (eYFP; $N = 19$ mice). The AAV reliably drove eYFP expression in an area generally well restricted to the nBIC/ECIC (although we cannot exclude the possibility that the most lateral part of the SGI was partially also hit, Fig. 2*A*). In order to test whether ChR2 was inserted into the membranes of the nBIC/ECIC neurons, we recorded from both nBIC and ECIC neurons and optically stimulated locally over their somata and proximal dendrites (Fig. 2*B*). At lower intensities (Fig. 2*B*, top), we were able to induce inward currents in voltage-clamp (Fig. 2*B*, left) as well as depolarizing potentials in current-clamp (Fig. 2*B*, right) with nearly no latency, and at higher intensities, larger currents were able to reliably evoke an AP (Fig. 2*B*, right bottom). The laser intensity that evoked spikes in nBIC/ECIC neurons was 35 ± 14 μW (mean $\pm$ SEM, $n =$ 10 nBIC/ECIC neurons). We found no differences in the laser intensity evoking spikes in nBIC or in ECIC neurons (nBIC 19 ± 8 μW, $n = 5$, ECIC 50 ± 27 μW, $n = 5$, $P =$ 0.83, Kruskal–Wallis test). While single-cell eYFP.ChR2 positivity is difficult to see in the confocal overview image (Fig. 2*A*), the somatic eYFP expression is easily detected under the two-photon microscope (Fig. 2*C*).

To probe the functional connectivity between the nBIC/ECIC and the neurons in the SGP, we optically activated the presynaptic axons running towards the SGP

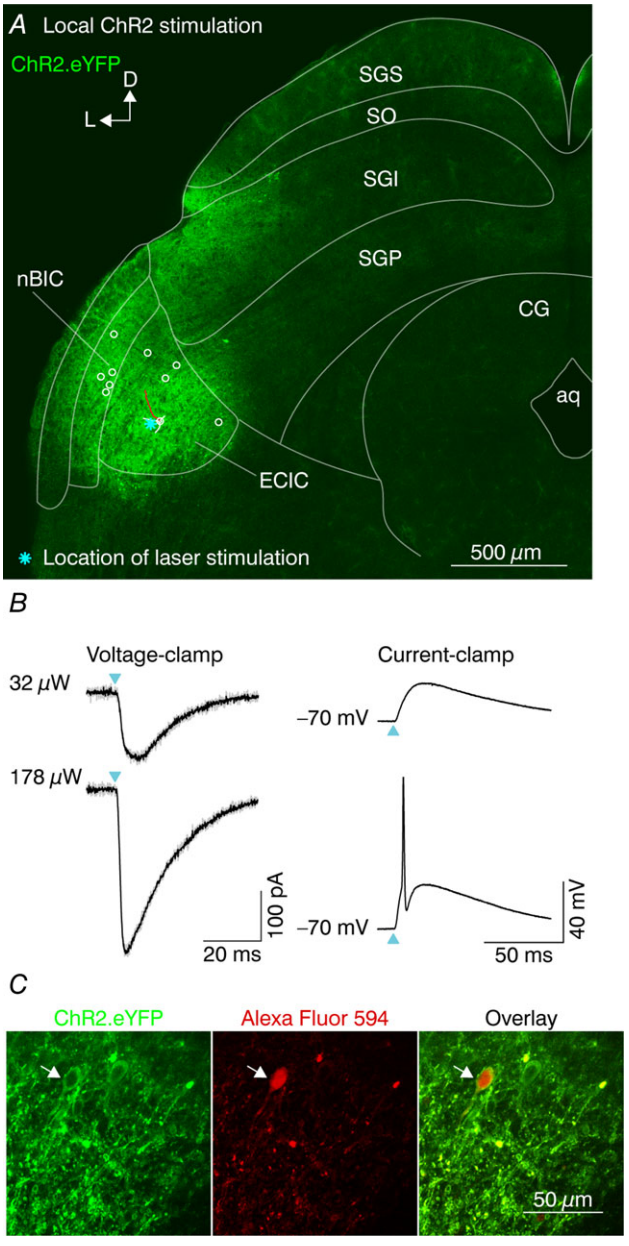

Figure 2. Optical activation of ChR2-positive neurons in the nBIC/ECIC
A, confocal image of a brain slice showing eYFP fluorescence in the nBIC/ECIC. An example ECIC neuron was partially traced (white lines, dendrites and soma; red line, axon). Locations of all nBIC ($n = 5$) and ECIC ($n = 5$) neurons are shown with open circles. Cyan asterisk shows the laser position for an example ECIC recording shown in *B*. *B*, example recording of local ChR2 stimulation. Voltage-clamp (left, $V_{holding} = -70$ mV) and current-clamp (right) recordings of an ECIC neuron at low (top) and high (bottom) laser intensities. Cyan triangles indicate the laser onset. Grey and black traces represent individual trials and the average, respectively. *C*, two-photon images of a recorded neuron located in the ECIC (white arrow) showing ChR2.eYFP fluorescence (left), Alexa Fluor 594 fluorescence (middle) filled via the patch pipette, and their overlay (right).

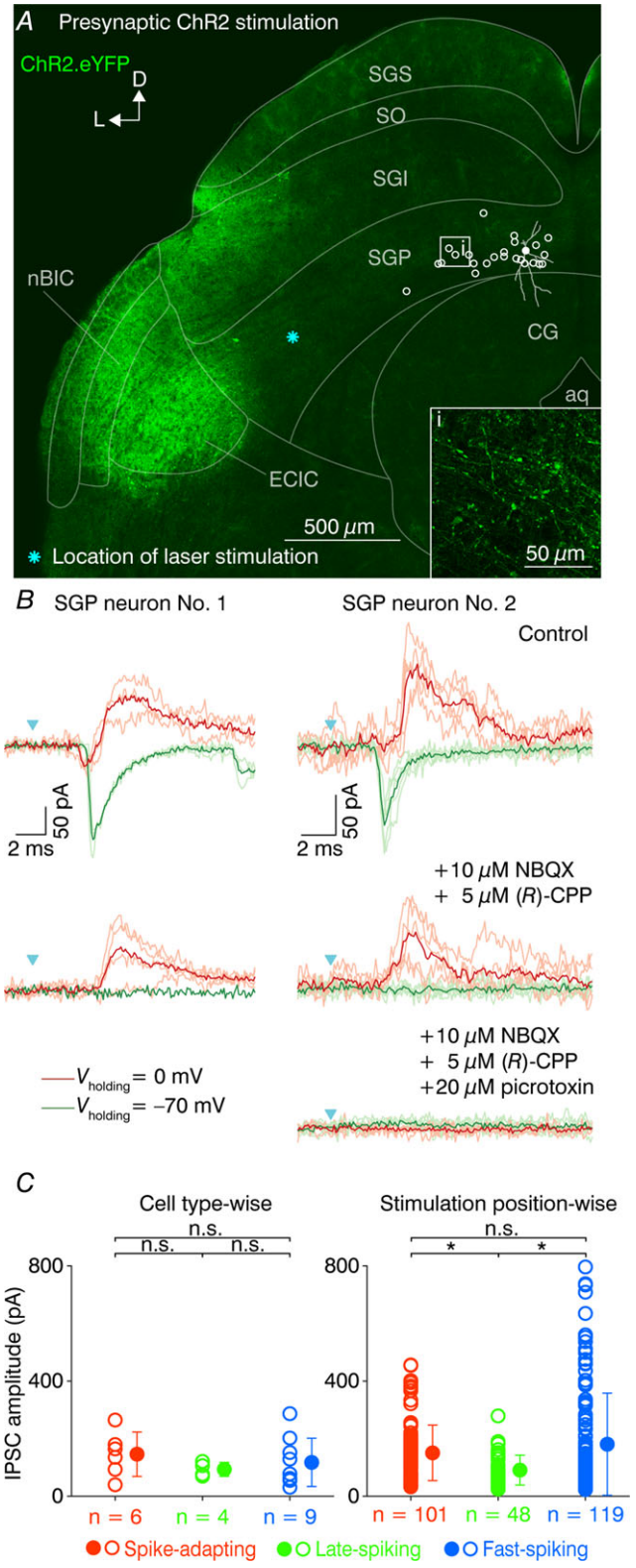

Figure 3. Optical activation of ChR2-positive axons in the nBIC/ECIC–SGP circuit
A, confocal image of a brain slice showing ChR2.eYFP fluorescence in the nBIC/ECIC. Higher magnification reveals eYFP-positive axons projecting into the SGP (inset). In presynaptic ChR2 stimulation, the locations of all recorded SGP neurons are shown by open circles. The filled circle denotes an SGP neuron whose voltage-clamp recordings are presented in (*B*, left). Cyan asterisk shows the laser position. *B*, voltage-clamp recordings of two SGP neurons and presynaptic ChR2 stimulation. An EPSC (green traces, $V_{holding} = -70$ mV) and an IPSC (red traces, $V_{holding} = 0$ mV) were recorded in control conditions (top), after NBQX and (*R*)-CPP wash-in (middle), and after picrotoxin wash-in (bottom, right). Lighter and darker traces represent individual trials and averages, respectively. Cyan triangles indicate the laser onset. Key applies to both recordings. *C*, strength of direct inhibition on SGP neurons cell type-wise and stimulation position-wise. The open circles in the cell type-wise plot (left) show average IPSC amplitude of a given SGP neuron, and the filled circles show the cell cluster mean ± SD. In the stimulation position-wise plots (right), the open and filled circles denote the IPSC amplitude of a given stimulation position and their mean ± SD, respectively. $^*P < 0.05$; n.s., not significant (two-sample Kolmogorov–Smirnov test).

while recording postsynaptic currents in SGP neurons that were voltage-clamped, allowing excitatory and inhibitory inputs to be probed in the same recording ($n = 25$, Fig. 3*A*). The eYFP signal was readily visible in both the nBIC and the ECIC, as well as in the axons projecting into the SGP (Fig. 3*A*, inset). Example recordings of two SGP neurons are shown in Fig. 3*B*. In one recording (Fig. 3*B*, left, filled circle in Fig. 3*A*) at a holding potential of −70 mV, near the reversal potential for chloride, we recorded an EPSC with a latency of 3.6 ± 0.1 ms (mean ± SD, Fig. 3*B* top left, green traces), consistent with the previously reported direct excitatory projection (Skaliora *et al.* 2004). At 0 mV, the approximate reversal potential for glutamate, we observed a small residual inward current followed by an IPSC with latency of 4.6 ± 0.38 ms, indicative of a polysynaptic inhibition (Fig. 3*B*, top left, red traces). To further investigate this possibility, we then added antagonists of NMDA and AMPA receptors (NBQX and (*R*)-CPP, respectively) into the bath to block any polysynaptically induced inhibition (Fig. 3*B*, middle left). Under these conditions, the EPSC was effectively abolished, but surprisingly, the IPSC (latency 4.5 ± 0.15 ms) remained, albeit with a slightly lower amplitude. In two further experiments we also added picrotoxin following the blockers of excitation, one of which is shown in Fig. 3*B*, right. All remaining currents were abolished (Fig. 3*B*, bottom right), thus confirming that the direct inhibition is indeed GABAergic. Importantly, this direct IPSC, to varying extents, was observed in 100% of SGP neurons recorded, irrespective of the electrophysiological cluster they were classified into. Thus, in addition to the previously described excitatory pathway, more than one type of inhibitory connection comprises the nBIC/ECIC–SGP input circuitry.

While the presence of direct inhibitory input to the SGP is irrefutable under conditions where excitation is blocked, the precise contribution of the polysynaptic inputs was less trivial to calculate. This is because trial-by-trial amplitude fluctuations were too large to accurately quantify differences in IPSC amplitudes

between the mixed (control) and direct-only (excitatory block) conditions. To obtain a rough picture of the prominence of polysynaptic inputs in our neuronal population, we simply performed Kruskal–Wallis tests, comparing IPSC amplitudes before and after blocking the excitation (Fig. 2*B*, comparison of the peaks in the top and bottom left red traces), and this was done for all laser stimulation positions in which the IPSCs exceeded 7 times the SD of the baseline. Here, we regarded recordings where blocking excitation significantly decreased the IPSC amplitude ($P < 0.05$, Kruskal–Wallis test) as polysynaptic containing connections (30/346 positions) and the number of neurons in which we calculated at least one such a connection was 15 out of 25 SGP neurons. On the other hand, the IPSCs where blocking excitation did not decrease IPSC amplitude were considered direct inhibition-dominated (316/346 positions). Thus, under our experimental conditions, the magnitude of the polysynaptic inhibition was small (9% out of all positions) in comparison to the striking direct inhibition (91% out of all positions).

Out of the 25 SGP neurons with confirmed direct inhibitory connection, we were able to obtain intrinsic electrophysiological recordings of 19 of them and thus analysed the data using hierarchical clustering as in Fig. 1*C*. To evaluate the strength of the direct inhibition on each of the three electrophysiological clusters, we plotted the direct inhibitory peak values cell type-wise and stimulation position-wise for all 19 SGP neurons (Fig. 3*C*). In the cell type-wise plots (Fig. 3C, left), the spike-adapting neurons had on average (mean ± SD) 146.4 ± 77.1 pA, the late-spiking 93.5 ± 24.3 pA, and fast-spiking 117.7 ± 83.9 pA IPSC peak amplitudes and their distributions were not different from each other (spike-adapting *vs.* late-spiking, $P = 0.14$; late-spiking *vs.* fast-spiking, $P = 0.53$; adapting *vs.* fast, $P = 0.51$; two-sample Kolmogorov–Smirnov test). Analysis of the IPSC amplitudes stimulation position-wise (Fig. 3C, right) revealed significant differences in the distributions of late-spiking (91.0 ± 51.7 pA, $n = 101$) to spike-adapting (150.8 ± 96.5 pA, $n = 48$, $P = 0.0003$, two-sample Kolmogorov–Smirnov test) and fast-spiking neurons (180.9 ± 177.3 pA, $n = 119$, $P = 0.003$, two-sample Kolmogorov–Smirnov test), but not between spike-adapting and fast-spiking neurons ($P = 0.23$, two-sample Kolmogorov–Smirnov test). Thus, the position-wise analysis indicates that late-spiking neurons receive weaker direct inhibition compared to their spike-adapting and fast-spiking counterparts. However, the fact that the cell-wise analysis, though exhibiting the same trends, returned no statistically significant difference between cell types, we conclude that all cell types receive similar levels of direct inhibition. Nevertheless, because of the presence of the direct inhibition in all SGP neurons recorded, we focused the rest of the study on the functional and anatomical organization of this ubiquitous connection.

We first wondered whether the excitatory and inhibitory axons originate from the same areas and whether they fasciculate tightly with one another within the nBIC/ECIC. To test this, we used ChR2-assisted circuit mapping (Petreanu *et al.* 2007) to locate the excitatory and the inhibitory axons in the nBIC/ECIC. For this purpose, we created a grid of 8 × 8 laser stimulation sites with 175 μm spacing. The stimulation grid covered both the nBIC and the ECIC, spanning a 1.2 × 1.2 mm large region from the lateral slice edge to the CG (Fig. 4*A*). To be sure that we stimulated distal nBIC/ECIC inputs of the SGP neurons, we recorded from SGP neurons located at least 400 μm from the medial edge of the grid ($n = 10/25$ SGP neurons; SGP neurons were located outside of the area shown in Fig. 4*A* and were clustered around the medial quarter of the SGP). Recordings of three representative neurons (out of 10 SGP neurons) were analysed and are shown as input heat maps in Fig. 4*B–D*. Here, the EPSCs and IPSCs evoked by laser stimulation at individual grid locations were used to construct excitatory ($V_{\text{holding}} = -70$ mV, Fig. 4*B–D*, top) and inhibitory ($V_{\text{holding}} = 0$ mV, Fig. 4*B–D*, bottom) input maps in control conditions (Fig. 4*B–D*, left). In each input map, individual squares represent an average (from 3 repetitions) of the peak PSC for that particular position. In order to differentiate the locations of the direct inhibitory inputs from the trajectories of the excitatory inputs, we repeated the maps in the presence of NBQX and (*R*)-CPP (Fig. 4*B–D*, right), thereby also eliminating the polysynaptic inhibitory components. Each map was then normalized to the maximum peak value of the control condition. For excitation, all maps in the drugs condition became zero by design. Responses in the inhibitory maps persisted, reflecting the direct, monosynaptic inhibitory projections, although slightly more broadly distributed compared to control conditions that contain both mixed and direct inhibition. This subtle difference is likely due a threshold artefact, whereby the blockers of excitatory transmission increased the input resistance during the IPSC thereby pushing small subthreshold events above our detection threshold. Non-normalized input map current mean and maximum (max) values were as follows: Fig. 4*B*, mean ± SEM, control excitation 41.1 ± 17.7 pA, max 72.1 pA; control inhibition 83.0 ± 52.8 pA, max 244.2 pA; drugs inhibition 61.8 ± 23.7 pA, max 132.9 pA; Fig. 4*C*, control excitation 48.0 ± 22.8 pA, max 143.7 pA; control inhibition 43.5 ± 12.0 pA, max 68.7 pA; drugs inhibition 39.1 ± 14.8 pA, max 83.6 pA; Fig. 4*D*, control excitation 118.0 ± 93.6 pA, max 283.8 pA; control inhibition 90.0 ± 29.3 pA, max 135.8 pA; drugs inhibition 81.6 ± 45.6 pA, max 164.2 pA. Already from these basic analyses, it is visually apparent that while the excitation was more broadly distributed, the direct inhibition seemed confined to the dorso-medial location within the stimulus grid.

To generalize these findings, we averaged the data from excitatory input maps in the control condition and the inhibitory input maps in the drugs condition for 10 SGP neurons (Fig. 5*A*). In general, the strongest responses were observed at positions closer to the recorded neuron. This is to be expected as fibres are less likely to be cut in areas closer to their targets. However, when comparing the direct excitatory and inhibitory distributions, the IPSCs were nearly exclusively induced from the medial extent of the dorsal part of the grid (red colour-scaled circles, Fig. 5*A*, left). In contrast, the EPSCs could be detected in SGP neurons by stimulation across the mediolateral extent of the dorsal part of the grid (green colour-scaled circles, Fig. 5*A*, right).

To quantify these differences, we took two approaches. In the first, we performed Kruskal–Wallis tests on the excitatory and inhibitory responses for each stimulation grid position and plotted the *P*-values as a heat map (Fig. 5*B*, $n = 10$ SGP neurons). Multiple positions in the dorsolateral part of the grid were found to be statistically different between excitation and inhibition in these regions.

In the second approach, we calculated the input distributions for all 10 SGP neurons recorded along the dorsoventral or mediolateral axes (Fig. 5*C*). In the dorsoventral distribution (Fig. 5C, left), both the direct and mixed inhibitory as well as excitatory distributions were similar, with most inputs located in the dorsal parts of the nBIC/ECIC. In the mediolateral distribution, however, there was a clear medial bias of the direct inhibitory connections compared to their excitatory counterparts (Fig. 5*C*, right). We then generated cumulative histograms of the data along each axis and performed non-parametric statistical analysis on the distribution of their half-maximal positions. Indeed, half-maximal positions from the dorsal slice edge in the dorsoventral axis between direct excitation (control excitation, 294.2 ± 56.7 μm) and mixed inhibition (control inhibition, 309.1 ± 100.5 μm) as well as direct inhibition (drugs inhibition, 209.9 ± 50.5 μm) were not significant ($P = 0.706$ and $P = 0.326$, respectively, Kruskal–Wallis test), reflecting the fact that in all cases the strongest input came from the dorsal region of the stimulus grid (to be expected as slicing generally preserves axons closer to their targets). In contrast, in the mediolateral axis both mixed and direct inhibition exhibited half-maximal positions significantly more medial (909.7 ± 55.1 and 926.2 ± 43.6 μm from the lateral slice edge, respectively)

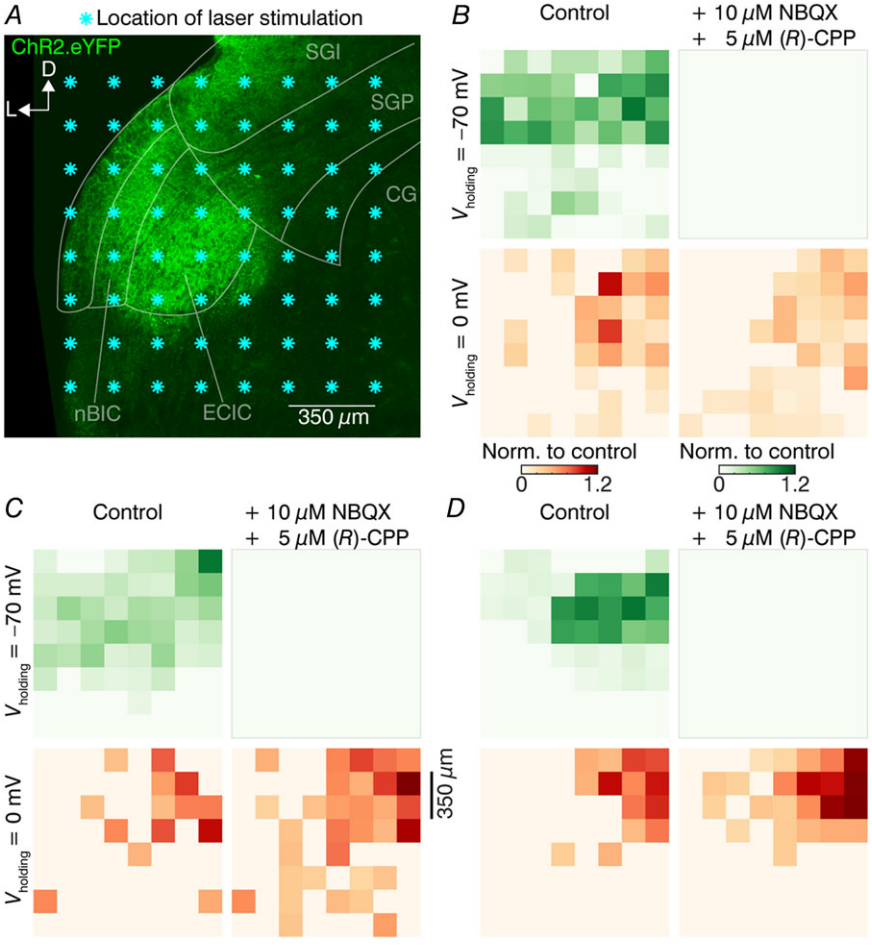

Figure 4. ChR2-assisted circuit mapping of the nBIC/ECIC–SGP circuit
A, confocal eYFP image of a brain slice with the mapped area covering the nBIC/ECIC for the example SGP neuron recording in *B*. Each asterisk indicates a location of the laser stimulation grid. Recorded neurons were located at least 400 μm dorsomedially from the nearest stimulation point. *B–D*, excitatory ($V_{holding} = -70$ mV, top) and inhibitory ($V_{holding} = 0$ mV, bottom) input maps created from voltage-clamp recordings for three example SGP neurons. Left and right maps were recorded in control conditions and in the presence of the drugs, respectively. All values are normalized to the maximum value of their respective control condition maps. Note that the post-drugs excitatory maps (upper right map) are by definition zero as excitation was pharmacologically blocked.

compared to direct excitation (749.2 ± 40.1 μm, P = 0.041 and P = 0.013, respectively, Kruskal–Wallis test), reflecting the fact that in the dorsolateral region of the grid the excitation was substantially stronger. Importantly, there were no statistically significant differences in the half-maximal positions along the dorsoventral (P = 0.545, Kruskal–Wallis test) as well as the mediolateral (P = 0.791, Kruskal–Wallis test) axes between mixed inhibition and the direct inhibition. Thus, broadening of input maps after the application of excitatory blockers as observed in Fig. 4*B–D* did not change the spatial distribution of inhibitory inputs on average.

Given such a robust spatial separation between excitatory and inhibitory inputs to the SGP, we were interested to see whether such trajectory differences would be reflected in the synaptic latency. Therefore, we calculated mean latency of the control excitatory and the drugs inhibitory maps for grid positions within the nBIC/ECIC in which both IPSCs and EPSCs were evoked (control excitation mean ± SEM, 5.78 ± 1.15 ms, drugs inhibition 4.56 ± 0.60 ms, n = 5 out of 10 SGP neurons which met the criteria, P = 0.451, paired two-tailed t test). Thus, despite the more medially located direct inhibitory inputs, their position-matched latencies were comparable to the direct excitatory inputs, at least at the level of the nBIC/ECIC, which suggests that excitatory and inhibitory inputs take functionally equivalent path lengths to their target neurons in the SGP.

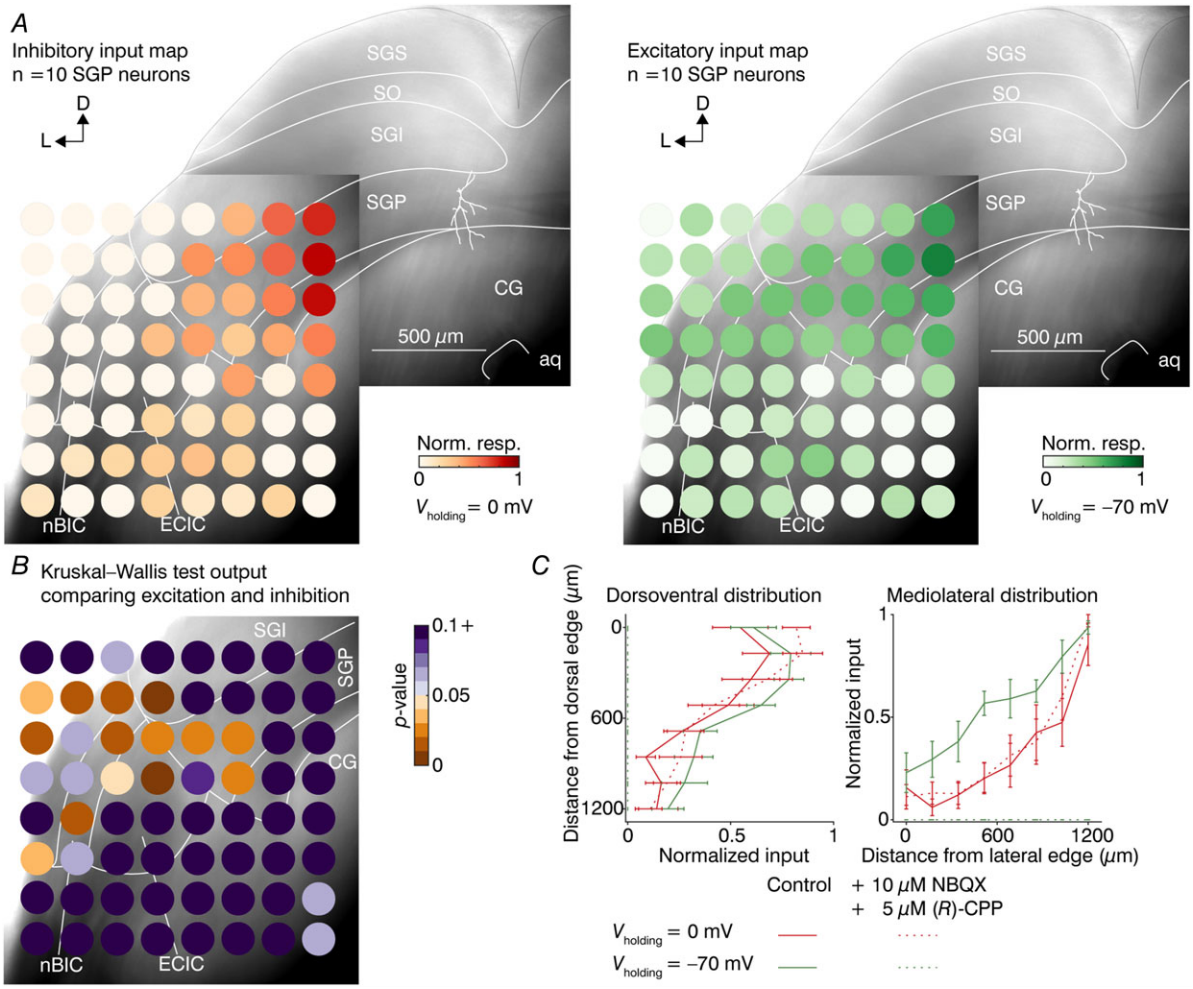

Figure 5. Mapping the locations of the excitatory and the inhibitory nBIC/ECIC inputs to SGP neurons
A, montage of two Dodt gradient contrast images with direct inhibitory (left) and excitatory (right) input maps averaged for 10 SGP neurons. Each circle represents the mean (n = 10 neurons) of the non-zero post-drugs inhibitory responses (left, red colour scale) and control excitatory responses (right, green colour scale). An example traced neuron (white lines) in the SGP is shown for orientation. Note that in this case, the inhibition was normalized to the drugs condition. *B*, Dodt gradient contrast image with heat map of *P*-values calculated by performing position-wise Kruskal–Wallis tests on the direct inhibitory and excitatory values of data shown in *A*. *C*, quantification of the input distributions in the dorsoventral (left) and mediolateral (right) axes, averaged across 10 SGP neurons. Each point along the line is the mean ± SEM of the maximal response for one of the eight dorsoventral and mediolateral positions relative to the edge of the slice.

Although the results from the ChR2-assisted circuit mapping experiments clearly show a trajectory bias of the inhibitory inputs toward the medial side, it is difficult to conclude whether the projection cell bodies are also differentially distributed within the nBIC/ECIC because ChR2 activation in both the axons and cell bodies can generate APs. Moreover, it was nearly impossible to avoid transducing the lateral part of the SGI/SGS of the SC while performing our injections. Although this represents at most five (of 64) positions on our stimulation grid (Fig. 3*A*), and our focal stimulation should not further spread into the SGI/SGS, we sought a complementary approach to corroborate these findings. We therefore used a tracing and histological approach to characterize the spatial distribution of SGP-projecting neuron somata within the nBIC/ECIC. Here, we injected a retrograde tracer into the SGP of the mouse SC ($N = 3$ mice) and performed an immunohistochemical analysis of the tracer-filled neurons in the nBIC/ECIC to gain insight into their neurochemical profiles (Fig. 6*A*). Examples of double-labelled neurons are presented in Fig. 6*B* and *C*. Although the total number of neurons retrogradely labelled in the nBIC was higher than in the ECIC (1389 in nBIC *vs.* 1112 in ECIC, Table 3), the percentage of those neurons positive for GAD67 was larger in the ECIC when compared to the nBIC (27% in ECIC *vs.* 7% in nBIC, 15% overall, Table 3) (Dillingham *et al.* 2017), providing evidence that cell bodies of SGP-projecting inhibitory neurons match the mediolateral axon trajectories (Fig. 5).

Table 3. Numbers and percentage of retrogradely labelled neurons GAD67 immunopositive

	nBIC	ECIC
Retro only (*n*)	1389	1112
Retro GAD67 (*n*)	95	235
% Retro GAD67	7	27

$N = 3$ mice; $n = 33$ nBIC/ECIC tiles.

Table 4. Numbers and percentage of retrogradely labelled neurons calretinin immunopositive

	nBIC	ECIC
Retro only (*n*)	427	411
Retro calretinin (*n*)	98	74
% Retro calretinin	30	22
Retro calretinin GAD67 (*n*)	0	0

$N = 3$ mice; $n = 11$ nBIC/ECIC tiles.

Moreover, retrogradely labelled neurons also positive for calretinin (although never also positive for GAD67; Dillingham *et al.* 2017) were distributed more equally throughout the nBIC and the ECIC regions (22% in ECIC *vs.* 30% in nBIC, Table 4), a finding also consistent with the more even distribution of the excitatory axon trajectories (Fig. 5). Thus, the histological analysis corroborated our electrophysiological experiments,

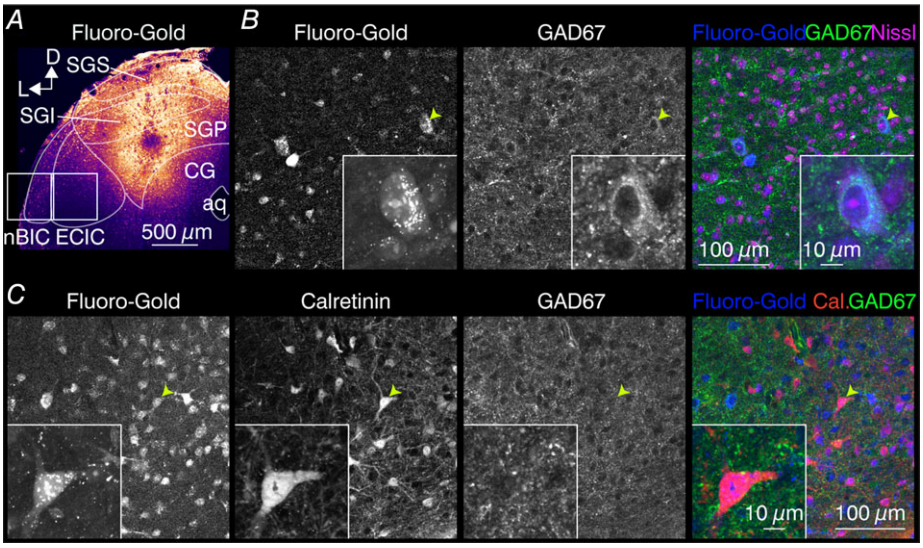

Figure 6. Retrogradely traced nBIC/ECIC neurons and their immunoreactivity for GAD67 and calretinin
A, confocal image of the Fluoro-Gold injection site in the SGP of the mouse SC. Retrogradely filled neurons were counted in the example highlighted tiles roughly corresponding to the nBIC and the ECIC. *B*, higher magnification images of a region within the ECIC with Fluoro-Gold filled neurons and their immunoreactivity for GAD67. Neuron highlighted by the arrow is shown in the inset. Data are summarized in Table 3. *C*, higher magnification images of a region within the nBIC with Fluoro-Gold filled neurons and their immunoreactivity for calretinin and GAD67. Neuron highlighted by the arrow (positive for calretinin, negative for GAD67) is shown in the inset. Data are summarized in Table 4.

Table 5. Numbers of retrogradely labelled cells calbindin immunopositive

	nBIC	ECIC
Retro only	140	118
Retro GAD67	15	30
Retro calbindin GAD67	2	2
Retro GAD67$^-$	125	88
Retro calbindin GAD67$^-$	31	14

$N = 2$ mice; $n = 4$ nBIC/ECIC tiles.

Table 6. Numbers of retrogradely labelled neurons parvalbumin immunopositive

	nBIC	ECIC
Retro only	454	261
Retro GAD67	20	61
Retro parvalbumin GAD67	17	44
Retro GAD67$^-$	434	200
Retro parvalbumin GAD67$^-$	9	3

$N = 3$ mice; $n = 11$ nBIC/ECIC tiles.

showing a distinct mediolateral distribution of SGP-projecting subpopulation of inhibitory neurons from their excitatory counterparts.

Finally, we investigated the identity of the direct inhibitory projection neurons in the nBIC/ECIC by co-staining for somatostatin, calbindin and parvalbumin with GAD67. Although we found no cells positive for somatostatin, we found a small proportion of SC-projecting inhibitory cells in the nBIC/ECIC to be positive for calbindin (nBIC, 2 out of 15 cells, 13%; ECIC, 2 out of 30 cells, 6%; Table 5). The majority of inhibitory cells in nBIC/ECIC that projected to the SC were parvalbumin positive (nBIC, 17 out of 20 cells, 85%; ECIC, 44 out of 61 cells, 72%; Table 6), although we also found a small proportion of GAD67-negative SC-projecting parvalbumin-positive neurons in both the nBIC and ECIC (nBIC, 9 out of 434 Retro GAD67-negative cells, 2%; ECIC, 3 out of 200 Retro GAD67-negative cells, 1.5%; Table 6). Thus, while the majority of SGP-projecting nBIC/ECIC inhibitory neurons are parvalbumin positive (with some calbindin exceptions), the identity of the remaining 16% of inhibitory neurons is yet to be determined.

Discussion

In this study, we characterized the electrophysiological profiles of neurons in the SGP layer of the SC in the mouse and the types of inputs they receive from the nBIC/ECIC. Electrophysiological and morphological profiling showed at least three types of neurons in the SGP consistent with types found in other SC layers. Surprisingly, each type of SGP neuron recorded from received a direct inhibitory connection in addition to a direct excitatory input. The excitation in some neurons drove feed-forward inhibition. We also found evidence for distinct axonal trajectories from the nBIC/ECIC to the SGP, corroborated by histological evidence supporting a difference in the locations of the excitatory and inhibitory projection neuron somata within the nBIC/ECIC.

Cell types within the SGP

While the SC of the mouse contains three distinguishable granular layers (SGS, SGI and SGP), most of the previous literature focused on the SGS and SGI and not the SGP. As it is unclear whether the SGP is purely sensory (like the SGS) or multisensory/premotor (like the SGI), comparisons with the SGS/SGI literature are relevant. Previous work from the Isa laboratory has described at least six electrophysiologically distinct classes of neurons in the SGI (Saito & Isa, 1999), three of which we also found in the SGP (late-spiking, spike-adapting, and fast-spiking). On the other hand, we did not encounter any burst-spiking or rapid-spike inactivation neurons in the SGP of the mouse SC. The majority of GABAergic neurons in the SGI were identified to be fast-spiking (Sooksawate *et al.* 2011), indicating that the fast-spiking neurons in the SGP could also be part of the intra- and interlaminar inhibitory SC circuitry. In addition, it has been postulated that the large multipolar regular-spiking neurons in the SGI serve the major motor output of the SC (Sooksawate *et al.* 2005). Anatomical studies have previously shown some multipolar neurons present in the SGP of the SC in the cat (Moschovakis & Karabelas, 1985), although it is unknown whether these neurons also project out of the SC. While we did not observe a cluster of regular-spiking neurons in the SGP of the mouse SC, we cannot exclude the possibility that a small population of these neurons also exists in the SGP.

Input circuitry from the nBIC/ECIC to the SGP

An anatomical examination of the connections between the nBIC/ECIC and the SC has been performed in a number of species (Druga & Syka, 1984; Covey *et al.* 1987; Jiang *et al.* 1997; King *et al.* 1998; Lesicko & Llano, 2018; Mellott *et al.* 2018). By injecting AAV.ChR2.eYFP into the nBIC/ECIC and then imaging the eYFP signal in fixed SC slices, we also confirm the anatomical projection from these auditory structures of the IC into the SGP layer of the SC in the mouse (Fig. 3*A*, injection site in the nBIC/ECIC and axons in the inset).

Electrical stimulation of the rat nBIC/ECIC showed an excitatory connection in the SGI (Skaliora *et al.* 2004). Our experimental protocol, using presynaptic activation of the nBIC/ECIC while recording in the SGP, extends these

findings. While we confirm the presence of an excitatory connection as described in the rat, we additionally describe a mixed polysynaptic and monosynaptic inhibition in this circuit (Fig. 7). The presence of the polysynaptic inhibition is perhaps not surprising as feed-forward inhibition is a common feature of input circuitry in many brain areas and was also described in the superficial and intermediate SC layers (Saito & Isa, 2003; Kardamakis *et al.* 2015). It is likely performed by the fast-spiking population of neurons in the SGP, as they are known to be GABAergic in the SGI (Sooksawate *et al.* 2011), but further experiments are required to address this question specifically (Fig. 7, dotted inhibitory synaptic connection in the SGP).

GABAergic projections from auditory structures to the SC have been described to originate in the ECIC of the cat (Appell & Behan, 1990) and in the nBIC of the guinea pig (Mellott *et al.* 2018), but in both cases the percentage of GABAergic neurons was rather small (only 10% in Mellott *et al.* 2018), and the studies therefore concluded that the contribution of direct inhibition to sensory processing in the SC was probably minor. Although our tracing data indicate comparably small percentages, we found that 100% of all SGP neurons we recorded from had direct inhibitory inputs. This indicates that although only a few inhibitory neurons in the nBIC/ECIC project directly to the SGP, their axonal arbours diverge massively to contact most, if not all neurons located in the medial part of the SGP of the mouse SC, suggesting that the functional implication of direct inhibition to the SGP might be more substantial than previously thought (Fig. 7, dotted inhibitory axonal collateral of the inhibitory neuron).

Our findings furthermore show that the majority of the nBIC/ECIC GABAergic cells also co-localizes with parvalbumin and to a very small extent with calbindin, while somatostatin was not detected at all in this region. Thus, identifying these inhibitory projection neurons revealed a subpopulation. Future experiments can target these projections in a cell type-specific manner for understanding the function of this direct inhibitory projection in the auditory circuit of the mouse SC.

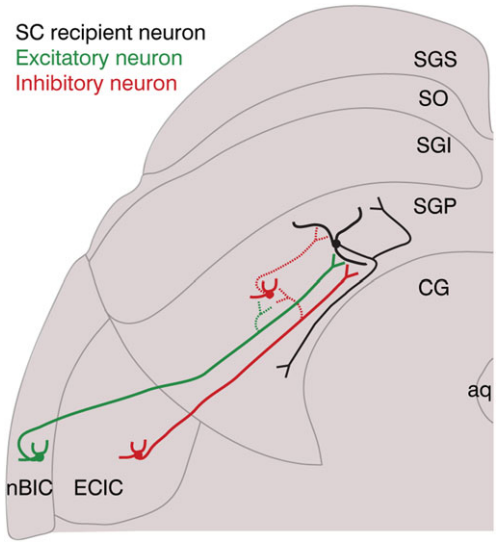

Figure 7. Proposed schema of the nBIC/ECIC projections into the mouse SC
In addition to a direct excitatory projection from the nBIC (green excitatory neuron) to the SGP-residing neuron (black), a direct inhibitory connection originating in the ECIC (red inhibitory neuron) is also present. Secondly, a feed-forward inhibitory connection is mediated by an axonal branch of the direct excitation (dotted green synapse) possibly involving an SGP-residing inhibitory interneuron (dotted inhibitory connection within the SGP). Thirdly, a direct inhibitory synapse (dotted red synapse) onto an SGP-residing inhibitory interneuron. Dotted synapses are only proposed. Note that the excitatory projection from the ECIC is not shown, and the inhibitory ECIC neuron presumably has more axonal collaterals than shown.

Spatially distinct excitatory and inhibitory inputs from the nBIC/ECIC to the SC

A particularly striking finding was the apparent difference in the mediolateral distribution between monosynaptic excitatory and inhibitory inputs from the nBIC/ECIC to the SGP. ChR2-assisted circuit mapping experiments revealed that at least inhibitory axon trajectories are relatively concentrated to the medial side. Retrograde tracing and immunohistochemical analysis further confirmed that the inhibitory projection cell bodies are also concentrated toward the medial side within the nBIC/ECIC. Because the ECIC is located slightly caudally to the nBIC, and because the nBIC/ECIC are generally caudal to the SGP neurons to which they project (Franklin & Paxinos, 2007), it is possible that the medial bias of axon trajectories in our slices reflects the medially projecting ECIC axons as they traverse rostrally through the slices we recorded from. This led us to conclude that the direct inhibitory input originates predominantly in the ECIC, whereas the excitatory inputs arise from both the nBIC and ECIC. It should, however, be noted that due to our strict distance requirement between stimulation and recording ($>400\ \mu$m), recordings for these experiments were restricted to the medial part of the SGP, and these interpretations may not fully generalize to the lateral segments of the SGP.

Another possible source of auditory inputs to the SC is the rostral pole of the IC (rpIC), as an anatomical projection from the rpIC has been characterized in the cat (Harting & Van Lieshout, 2000). Although the rpIC has been anatomically delineated in a Golgi study of the mouse (Meininger *et al.* 1986), its projections to the SC have not been characterized. Further investigations into the anatomical borders between nBIC, ECIC and rpIC, for example by single neuron tracing, will be necessary to disentangle the contribution of each of their projections to the SC.

Functional implications of a direct inhibitory nBIC/ECIC input to the SC

While it is generally accepted that feed-forward inhibition enforces a precise time window during which the post-synaptic neuron can be excited, the direct, long-range inhibitory projection we describe here enriches the patterning of input activity to the SGP. The fact that relatively few inhibitory neurons from the nBIC/ECIC project to most, if not all neurons in the medial SGP (the region we recorded from) indicates a broader divergence of these inputs compared to their excitatory counterparts. Interestingly, the nBIC/ECIC comprises GAD67-positive neurochemical modules, which are thought to receive axonal terminations predominantly from somatosensory structures (somatosensory cortex and dorsal column nuclei), while the auditory inputs (from the auditory cortex and the ICc) terminate in the extramodular zones (Lesicko *et al.* 2016). Furthermore, a recent study identified an excitatory auditory pathway from the ECIC extramodular zones to the SC in the mouse (Lesicko & Llano, 2018). Thus, it remains possible that the direct inhibitory inputs we recorded in the SGP carry a mix of auditory, somatosensory, or even multisensory information, while the excitatory/feed-forward inhibitory inputs are predominantly auditory in nature. It is tempting to speculate that the larger divergence of the direct inhibitory inputs underlies a specific coding strategy the SGP employs to interpret its sensory inputs. For example, it is known that the nBIC contains multiple classes of spatially tuned auditory responsive neurons that do not necessarily mirror those found in the SC (Schnupp & King, 1997). It is therefore possible that the SC refines its spatial tuning by drawing from the diversity of excitatory and inhibitory inputs from the nBIC/ECIC. Future *in vivo* studies of this complex circuitry thus have promise to disentangle the functional implications of its individual components for sensory integration and multimodal processing in the SC.

References

Ahmadlou M & Heimel JA (2015). Preference for concentric orientations in the mouse superior colliculus. *Nat Commun* **6**, 6773.

Aitkin LM & Phillips SC (1984). The interconnections of the inferior colliculi through their commissure. *J Comp Neurol* **228**, 210–216.

Appell PP & Behan M (1990). Sources of subcortical GABAergic projections to the superior colliculus in the cat. *J Comp Neurol* **302**, 143–158.

Chevalier G & Mana S (2000). Honeycomb-like structure of the intermediate layers of the rat superior colliculus, with additional observations in several other mammals: AChE patterning. *J Comp Neurol* **419**, 137–153.

Covey E, Hall WC & Kobler JB (1987). Subcortical connections of the superior colliculus in the mustache bat, *Pteronotus parnellii*. *J Comp Neurol* **263**, 179–197.

Dillingham CH, Gay SM, Behrooz R & Gabriele ML (2017). Modular-extramodular organization in developing multisensory shell regions of the mouse inferior colliculus. *J Comp Neurol* **525**, 3742–3756.

Doubell TP, Baron J, Skaliora I & King AJ (2000). Topographical projection from the superior colliculus to the nucleus of the brachium of the inferior colliculus in the ferret: Convergence of visual and auditory information. *Eur J Neurosci* **12**, 4290–4308.

Druga R & Syka J (1984). Projections from auditory structures to the superior colliculus in the rat. *Neurosci Lett* **45**, 247–252.

Edwards SB, Ginsburgh CL, Henkel CK & Stein BE (1979). Source of subcortical projections to the superior colliculus in the cat. *J Comp Neurol* **184**, 309–330.

Feinberg EH & Meister M (2015). Orientation columns in the mouse superior colliculus. *Nature* **519**, 229–232.

Franklin K & Paxinos G (2007). *The Mouse Brain in Stereotaxic Coordinates*, 3rd edn. Elsevier, New York.

Gale SD & Murphy GJ (2014). Distinct representation and distribution of visual information by specific cell types in mouse superficial superior colliculus. *J Neurosci* **34**, 13458–13471.

Gale SD & Murphy GJ (2016). Active dendritic properties and local inhibitory input enable selectivity for object motion in mouse superior colliculus neurons. *J Neurosci* **36**, 9111–9123.

Grundy D (2015). Principles and standards for reporting animal experiments in *The Journal of Physiology* and *Experimental Physiology*. *J Physiol* **593**, 2547–2549.

Harting JK & Van Lieshout DP (2000). Projections from the rostral pole of the inferior colliculus to the cat superior colliculus. *Brain Res* **881**, 244–247.

Helms MC, Özen G & Hall WC (2004). Organization of the intermediate gray layer of the superior colliculus. I. Intrinsic vertical connections. *J Neurophysiol* **91**, 1706–1715.

Inayat S, Barchini J, Chen H, Feng L, Liu X & Cang J (2015). Neurons in the most superficial lamina of the mouse superior colliculus are highly selective for stimulus direction. *J Neurosci* **35**, 7992–8003.

Jiang ZD, Moore DR & King AJ (1997). Sources of subcortical projections to the superior colliculus in the ferret. *Brain Res* **755**, 279–292.

Kardamakis AA, Saitoh K & Grillner S (2015). Tectal microcircuit generating visual selection commands on gaze-controlling neurons. *Proc Natl Acad Sci U S A* **112**, 1956–1965.

King AJ & Hutchings ME (1987). Spatial response properties of acoustically responsive neurons in the superior colliculus of the ferret: a map of auditory space. *J Neurophysiol* **57**, 596–624.

King AJ, Jiang ZD & Moore DR (1998). Auditory brainstem projections to the ferret superior colliculus: Anatomical contribution to the neural coding of sound azimuth. *J Comp Neurol* **390**, 342–365.

Lesicko AMH, Hristova TS, Maigler KC & Llano DA (2016). Connectional modularity of top-down and bottom-up multimodal inputs to the lateral cortex of the mouse inferior colliculus. *J Neurosci* **36**, 11037–11050.

Lesicko AMH & Llano DA (2018). Neurons projecting from the lateral cortex of the inferior colliculus to the superior colliculus are found in auditory-recipient extra-modular zones PS 51. 41st Annual MidWinter Meeting, Association for Research in Otolaryngology, pp. 29–30.

May PJ (2005). The mammalian superior colliculus: Laminar structure and connections. *Prog Brain Res* **151**, 321–378.

Meininger V, Pol D & Derer P (1986). The inferior colliculus of the mouse. A Nissl and Golgi study. *Neuroscience* **17**, 1159–1179.

Mellott JG, Beebe NL & Schofield BR (2018). GABAergic and non-GABAergic projections to the superior colliculus from the auditory brainstem. *Brain Struct Funct* **223**, 1923–1936.

Middlebrooks C & Knudsen EI (1984). A neural code for auditory space in the cat's superior colliculus. *J Neurosci* **4**, 2621–2634.

Moschovakis AK & Karabelas AB (1985). Observations on the somatodendritic morphology and axonal trajectory of intracellularly HRP-labeled efferent neurons located in the deeper layers of the superior colliculus of the cat. *J Comp Neurol* **239**, 276–308.

Nathanson JL, Yanagawa Y, Obata K & Callaway EM (2009). Preferential labelling of inhibitory and excitatory cortical neurons by endogenous tropism of adeno-associated virus and lentivirus vectors. *Neuroscience* **161**, 441–450.

Palmer AR & King AJ (1982). The representation of auditory space in the mammalian superior colliculus. *Nature* **299**, 248–249.

Petreanu L, Huber D, Sobczyk A & Svoboda K (2007). Channelrhodopsin-2-assisted circuit mapping of long-range callosal projections. *Nat Neurosci* **10**, 663–668.

Petreanu L, Mao T, Sternson SM & Svoboda K (2009). The subcellular organization of neocortical excitatory connections. *Nature* **457**, 1142–1145.

Saito Y & Isa T (1999). Electrophysiological and morphological properties of neurons in the rat superior colliculus. I. Neurons in the intermediate layer. *J Neurophysiol* **82**, 754–767.

Saito Y & Isa T (2003). Local excitatory network and NMDA receptor activation generate a synchronous and bursting command from the superior colliculus. *J Neurosci* **23**, 5854–5864.

Schnupp JW & King AJ (1997). Coding for auditory space in the nucleus of the brachium of the inferior colliculus in the ferret. *J Neurophysiol* **78**, 2717–2731.

Sholl BDA (1953). Dendritic organization in the neurons of the visual and motor cortices of the cat. *J Anat* **87**, 387–407.

Skaliora I, Doubell TP, Holmes NP, Nodal FR & King AJ (2004). Functional topography of converging visual and auditory inputs to neurons in the rat superior colliculus. *J Neurophysiol* **92**, 2933–2946.

Sooksawate T, Isa K, Behan M, Yanagawa Y & Isa T (2011). Organization of GABAergic inhibition in the motor output layer of the superior colliculus. *Eur J Neurosci* **33**, 421–432.

Sooksawate T, Saito Y & Isa T (2005). Electrophysiological and morphological properties of identified crossed tecto-reticular neurons in the rat superior colliculus. *Neurosci Res* **52**, 174–184.

Suter B, O'Connor T, Iyer V, Petreanu L, Hooks B, Kiritani T, Svoboda K & Sheperd G (2010). Ephus: multipurpose data acquisition software for neuroscience experiments. *Front Neural Circuits* **4**, 100.

Additional information

Competing interests

The authors declare no competing financial interests.

Author contributions

The experiments were carried out at the Max Planck Institute of Neurobiology at the Max Planck Fellow Group: Circuits of Spatial Hearing. All authors contributed to conception or design of the work, acquisition, analysis or interpretation of data, and drafting the work or revising it critically for important intellectual content. All authors confirm that they approved the final version of the manuscript, agree to be accountable for all aspects of the work in ensuring that questions related to the accuracy or integrity of any part of the work are appropriately investigated and resolved, and all persons designated as authors qualify for authorship, and all those who qualify for authorship are listed.

Funding

This work was supported by the Max Planck Society (V.B., B.G., M.H.M.), Graduate School of Systemic Neurosciences (V.B., B.G., M.H.M.), and a Boehringer Ingelheim PhD fellowship to V.B.

Acknowledgements

We thank H. Wohlfrom and C. Kopp-Scheinpflug for help with retrograde tracing, S. Weiler, V. Scheuss, T. Rose and V. Staiger for help with the two-photon laser-stimulation set-up, and the Department Synapses–Circuits–Plasticity (T. Bonhoeffer) for generously providing space and infrastructure to carry out this study.